3D Printing of Luminescent Perovskite Quantum Dot–Polymer Architectures

Hongryung Jeon, Muhammad Wajahat, Seobin Park, Jaeyeon Pyo, Seung Kwon Seol, Namhun Kim, Il Jeon, and Im Doo Jung*

Organic–inorganic perovskite quantum dot (PQD)–polymer composites are emerging optoelectronic materials with exceptional properties that are promising widespread application in next-generation electronics. Advances in the utilization of these materials depend on the development of suitable fabrication techniques to create 3D architectures composed of PQD–polymer for sophisticated optoelectronics. This study introduces a straightforward and effective method for producing 3D architectures of PQD-encapsulated high-performance composites (PQD-HPCs) through direct-ink writing (DIW). This method employs an ink composed of prefabricated PQDs and hydroxypropyl cellulose (HPC) in dichloromethane (DCM). HPC, an appropriate organic-soluble polymer, exhibits optical transparency in the highly volatile DCM and enables the formulation of a stable, room-temperature extrudable ink. The architectures, which are printed by adjusting the halide ratios (Cl, Br, and I) for the compositions of $CH_3NH_3PbBr_{1.5}I_{1.5}$, $CH_3NH_3PbBr_3$, and $CH_3NH_3PbBr_{1.5}Cl_{1.5}$, exhibit single peak photoluminescence emissions of red (639 nm), green (515 nm), and blue (467 nm). Optimizing the printing parameters of DIW enables the precise fabrication of programmed and complex PQD-HPC 3D architectures for advanced anti-counterfeiting and information encryption. This method has the potential to enhance the functionality of modern printed electronic devices significantly.

H. Jeon, M. Wajahat, S. Park, N. Kim, I. D. Jung
Department of Mechanical Engineering
Ulsan National Institute of Science and Technology (UNIST)
Ulsan 44919, Republic of Korea
E-mail: idjung@unist.ac.kr

J. Pyo, S. K. Seol
Smart 3D Printing Research Team
Korea Electrotechnology Research Institute (KERI)
Changwon-si, Gyeongsangnam-do 51543, Republic of Korea

I. Jeon
Department of Nano Engineering
Department of Nano Science and Technology
SKKU Advanced Institute of Nanotechnology (SAINT)
Sungkyunkwan University (SKKU)
Suwon 16419, Republic of Korea

1. Introduction

Organic–inorganic methylammonium lead-halide $CH_3NH_3PbX_3$ (X = Cl, Br, and I) perovskite quantum dots (PQDs) are attractive optoelectronic materials with exceptional physical properties, such as high-photoluminescence (PL) quantum yield, color tunability, short-radiative lifetimes, narrow-band emissions, and solution processability.[1–5] PQDs have garnered considerable attention for a wide array of optoelectronic devices, including solar cells, light-emitting diodes, and photodetectors.[6–11] Typical fabrication methods of photonic and electronic devices rely on conventional patterning techniques that focus on the production of 2D designs on planar surfaces.[12–24] An intriguing strategy to advance optoelectronic circuitries and devices is by vertically stacking them in 3D on non-planar surfaces to achieve a large aspect ratio for improving geometric scalability, increasing device efficacy, and further benefit device-integration technologies.[25–27] Several anticipated applications in next-generation electronics include wearable sensors, displays, and biomedical and energy-conversion devices. The integration of optoelectronic components into 3D structures has the potential to improve the functionality of electronic devices in terms of their advanced electrical, optical, and mechanical properties.

3D Printing offers complex and free-form design features for the realization of 3D electronic devices.[28–32] Studies on the conventional fused-filament fabrication (FFF) process for producing 3D objects using perovskite photoluminescent materials have been reported. The FFF process relies on printing by melting thermoplastic-based binders such as polycaprolactone, polylactic acid, and acrylonitrile butadiene styrene.[33–36] Although perovskite nanoparticles-composites of these filament types can exhibit luminescent structures, thermal damage to perovskite materials is unavoidable during the melting process, which limits their luminescence properties including complex process in operating the filament extrusion system. Direct-ink writing (DIW) is an alternative approach to circumvent this problem. The DIW approach has shown progress in utilizing diverse classes of nanomaterials as printable inks, including PQDs, graphene, carbon nanotubes, metallic nanoparticles, and lithium-metal oxide

**ADVANCED
SCIENCE NEWS**

www.advancedsciencenews.com

**ADVANCED
FUNCTIONAL
MATERIALS**

www.afm-journal.de

nanoparticles.[37–40] Owing to its versatility in handling a broad range of materials, DIW is also widely used in 4D printing.[41–43]

The optimal formulation and processing route of stable viscoelastic inks for exceptional rheological performance have been achieved without altering the intrinsic attributes of 1D PQDs, which are effectively translated into their 3D-printed architecture. Pure PQDs exhibit high absorption and emission efficiency, promising application for optoelectronics and photovoltaics. However, they are susceptible to degradation upon exposure to heat and oxygen. The introduction of composites into PQDs enhances the overall stability, and mechanical strength and robustness of 3D-printed structures.[44] Several printing methods, such as inkjet,[45] laser writing,[46] and meniscus-assisted self-assembly,[47] have been explored to demonstrate the patterns of PQD-based structures. These methods enable the printing or patterning of microstructures with various functional inks.[48–50] Stable and flexible luminescent quantum dot/polymer matrix is demonstrated through direct ink writing.[51] As quantum dots undergo synthesis via a hot injection process and the printed structures are cured during long-time post-processing, these methods face technical challenges related to process complexity with a trade-off between printability and QD functionality. Nanopipettes have been particularly used to produce perovskite nanostructures by inducing the localized crystallization of precursor inks within a nanoscale meniscus.[52,53] The use of photoluminescent nanostructures can provide effective security features for anti-counterfeiting or information encryption.[54] However, the meniscus-confined crystallization approach may face challenges related to strict environmental control, such as humidity, and restricted design freedom for complex 3D volumetric printing owing to the wetting-based process. In this respect, the DIW of luminescent PQD provides simplicity and versatility in the fabrication process, contributing to the expansion of the applications of 3D-PQD architectures.

In this study, we have developed a novel approach for one-step fabrication of 3D luminescent complex volumetric architectures at room temperature using a methylammonium lead halide PQD-filled polymeric ink via DIW. The ink consisted of CH3NH3PbX3 (X = mixed halide anion) PQDs, hydroxypropyl cellulose (HPC), and dichloromethane (DCM). HPC, a polymer soluble in organic solvents, demonstrated optical transparency in highly volatile DCM. The HPC enables stable room-temperature nozzle extrusion. Multicolored inks of red, green, and blue (RGB) were prepared by varying the halide ratios (Cl, Br, and I), particularly CH3NH3PbBr1.5I1.5, CH3NH3PbBr3, and CH3NH3PbBr1.5Cl1.5. The developed method enabled continuous layering and printing of complex 3D models. By optimizing the printing parameters, the printability of programmed and intricate PQD–HPC architectures, such as pyramids or Eiffel towers, was successfully demonstrated with precise localization. The 3D printed PQD–HPC architectures were depicted as multiple, bicolor, 3D cubes for quadruple anti-counterfeiting and information encryption.
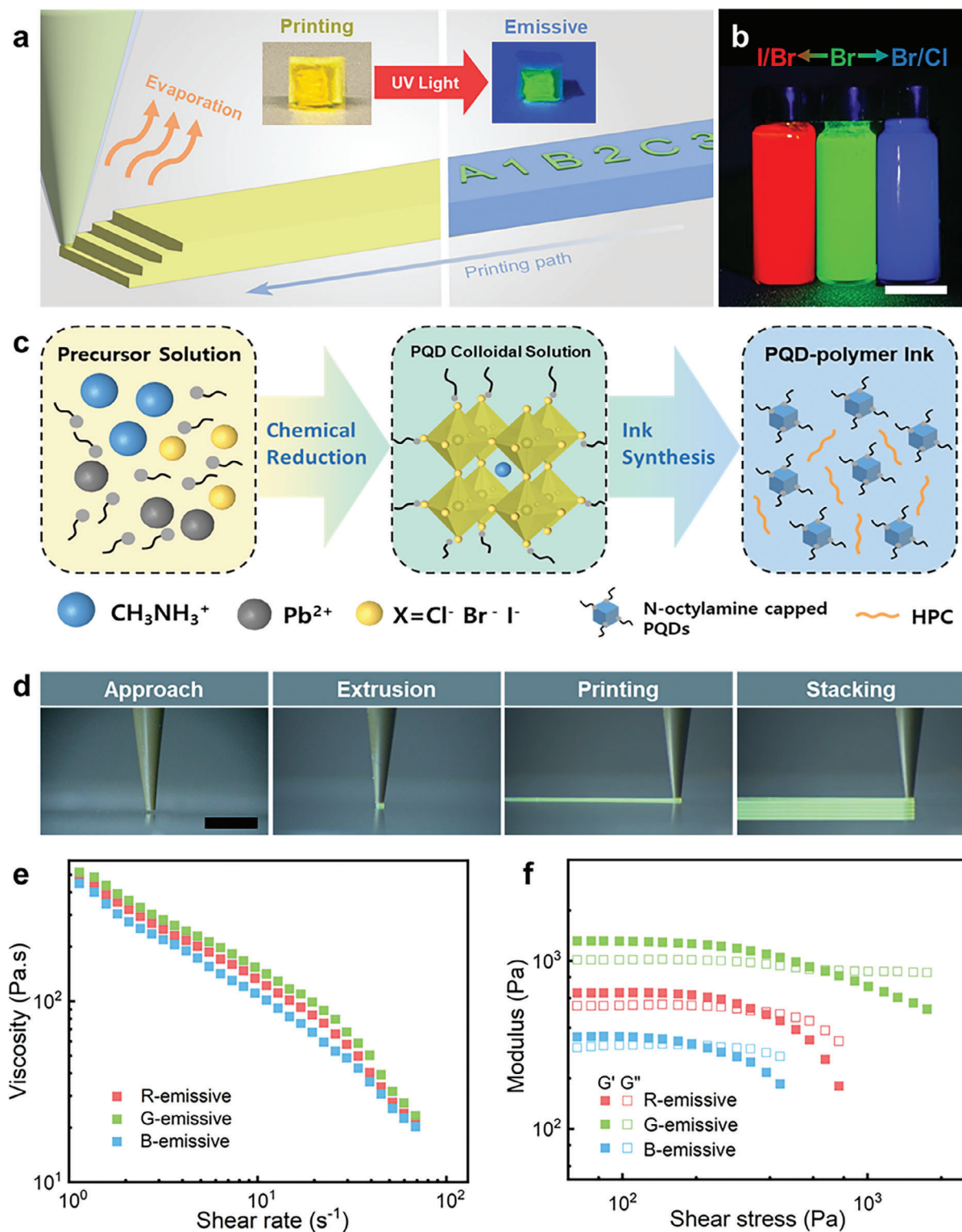
2. Results and Discussion

Figure 1a shows the layer-by-layer (LbL) PQD–polymer 3D printing for a bulk architecture. A micronozzle patterns the PQD-loaded polymeric ink containing a volatile solvent, where evap-
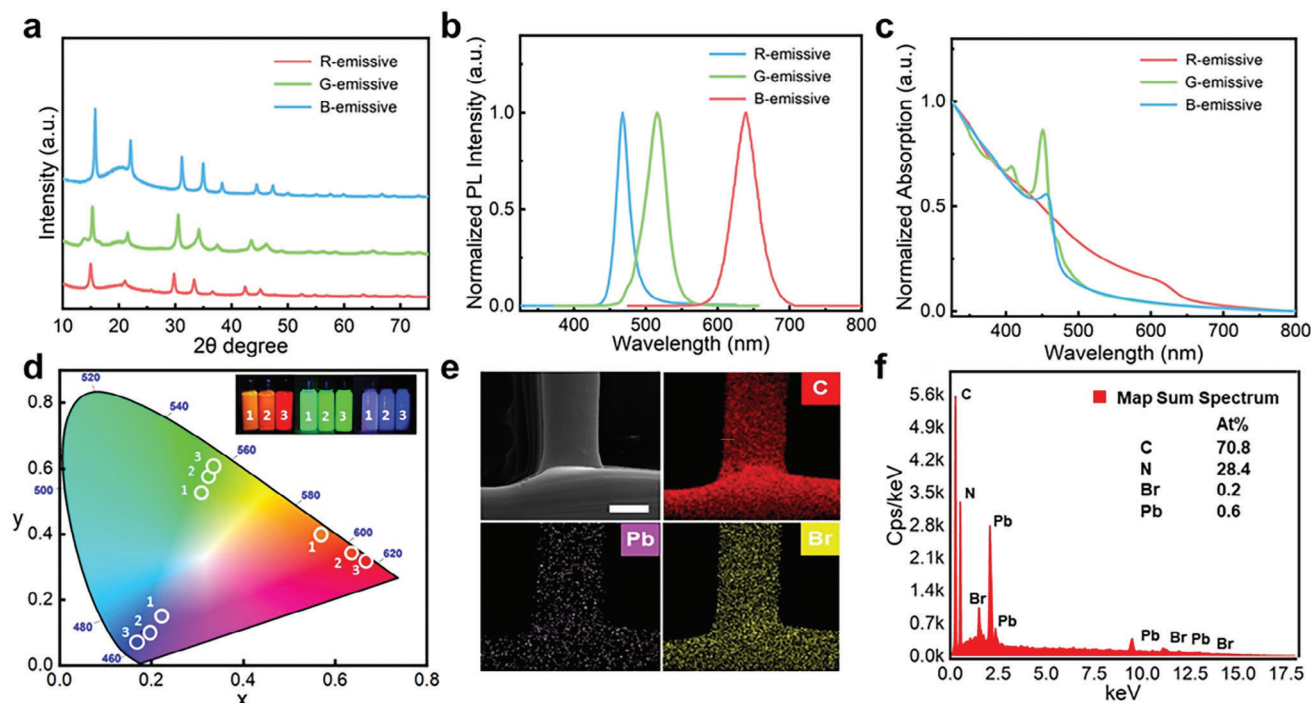
oration during printing forms the stacked architecture. The printed architecture emits distinct wavelengths after absorbing 385 nm ultraviolet (UV) light. Systematic, layer stacking allows distinctive features to be displayed under UV light within the multiple-array structure. The DIW technique relies on specific rheological characteristics in response to shear stress, transitioning between solid and fluid-like behaviors, which is crucial for facilitating the extrusion of the ink through a nozzle under applied pressure. The PQD–polymer inks exhibit RGB-emissive colors with respect to halide ratios of CH3NH3PbBr1.5I1.5, CH3NH3PbBr3, and CH3NH3PbBr1.5Cl1.5 in PQDs as visible under 385-nm UV light (the optical image in Figure 1b).

The synthesis of the luminescent PQD–polymer ink comprises two steps: 1) synthesis of PQDs by vigorously mixing a precursor solution of CH3NH3PbX3 in an antisolvent to prepare a colloidal dispersion solution, as schematically shown in Figure 1c and 2) addition of PQD into a HPC polymer dissolved in DCM to formulate the PQD–polymer inks. For the CH3NH3PbBr1.5Cl1.5 PQD–polymer ink, a precursor solution containing methylammonium bromide (CH3NH3Br), methylammonium chloride (CH3NH3Cl), lead bromide (PbBr2), and lead chloride (PbCl2) was dissolved in a mixture of N,N-dimethylformamide (DMF) and γ-butyrolactone (GBL) with a volume ratio of 1:20, along with n-octylamine. This mixture was then injected dropwise into stirred toluene to form a colloidal dispersion of methylammonium lead chloride/bromide PQD (CH3NH3PbCl1.5Br1.5 PQD), followed by the addition of HPC to quantum dot powder to prepare PQD–polymer inks. HPC is an organic soluble cellulose derivative that acts as a viscoelastic binder (Figure S1, Supporting Information).

Optical graphs of DIW of PQD–polymer inks dispensed through a micronozzle (inner diameter, ID = 150 μm) under an applied pressure (P) of 80 kPa are shown in Figure 1d. During the printing process, a continuous line pattern was deposited by precise horizontal movement (v_p = 0.1 mm s^{-1}) onto a glass substrate. The ink extruded by the micronozzle displays each emissive color according to the printed pattern (Figure S2, Supporting Information). The viscosity and moduli of the PQD–polymer ink, dependent on the shear stress and shear rate, are presented in Figure 1e,f. The inks exhibit apparent shear-thinning behavior, with high viscosity at low shear rates and low viscosity at high shear rates. As the shear rate increases from 10 to 10^1 s^{-1}, the viscosity decreases from 10^2 to 10^1 mPa·s, facilitating the extrusion of ink through a narrow micronozzle. Below the shear yield stress (≈10^2 Pa), the inks have a stable storage modulus (G') slightly above the loss modulus (G''), allowing the ink to maintain its shape after deposition. As the shear stress exceeds the yield point, the storage modulus drops below loss modulus (G' < G''), enabling the ink to flow at moderate pressures without the nozzle clogging. Increasing the content of HPC under the same PQDs conditions decreases the photoluminescent efficiency of PQD-polymer as HPC controls the amount of ink. Therefore, the rheological properties of ink are determined by the content of DCM. Incorporating a higher amount of DCM results in lower ink viscosity and loss modulus. This not only enables the ink to exhibit fluid-like properties under lower pressure, but also allows extrusion through a nozzle with a smaller diameter. However, the challenge with low-viscosity ink lies in the slower evaporation of the printed part, leading to difficulties in the layer-by-layer

**ADVANCED
SCIENCE NEWS**

www.advancedsciencenews.com

**ADVANCED
FUNCTIONAL
MATERIALS**

www.afm-journal.de

Figure 1. a) Schematic of the direct-ink writing (DIW) approach of luminescent PQD–polymer architectures. Hydroxypropyl cellulose (HPC) polymer was dissolved in DCM to prepare a 3D printable ink. b) Optical image of the inks as visible in 385-nm ultraviolet (UV) light. PQD–polymer inks display red (R), green (G), and blue (B) emissive colors, corresponding to the halide ratios of $CH_3NH_3PbBr_{1.5}I_{1.5}$, $CH_3NH_3PbBr_3$, and $CH_3NH_3PbBr_{1.5}Cl_{1.5}$. The scale bar is 5 mm. c) Schematic of the synthesis of luminescent PQDs as a colloidal dispersion solution in toluene, including the synthesis of PQD-polymer ink with HPC. d) Optical images of the DIW process show continuous deposition of a line pattern on the glass substrate. The scale bar is 1 mm. e) Rheological property depicts a decrease in the viscosity of the ink as the shear rate increases (shear-thinning behavior). f) Solid-like inks are shifted to a liquid-like fluid as a rheological function of the shear stress.

**ADVANCED
SCIENCE NEWS**

www.advancedsciencenews.com

**ADVANCED
FUNCTIONAL
MATERIALS**

www.afm-journal.de

Figure 2. Characteristics of R, G, and B-emissive PQD–HPC architectures. a) X-ray diffraction (XRD) patterns with respect to halide ratios of $CH_3NH_3PbBr_{1.5}I_{1.5}$, $CH_3NH_3PbBr_3$, and $CH_3NH_3PbBr_{1.5}Cl_{1.5}$ in the PQD–HPC film. The black diamond indicates the main diffraction peaks of $CH_3NH_3PbBr_3$ PQD–HPC. b) PL emission spectra and c) UV–vis absorption obtained of R, G, and B-emissive PQD–HPC. d) CIE chromaticity diagram showing color coordinates of the PQD–HPC compositions. Color differences in PQD–HPC ink with varying amounts of PQDs and constant amount of HPC solution (4 mL). The inset shows the optical image of PQD–HPC inks under 385-m UV-light excitation. e) SEM with EDS of elemental mapping and f) energy spectrum results of G-emissive ($CH_3NH_3PbBr_3$) PQD–HPC architecture. The scale bar is 50 μm.

stacking. The transition of solid- to fluid-like behaviors was required to produce 3D luminescent structures.
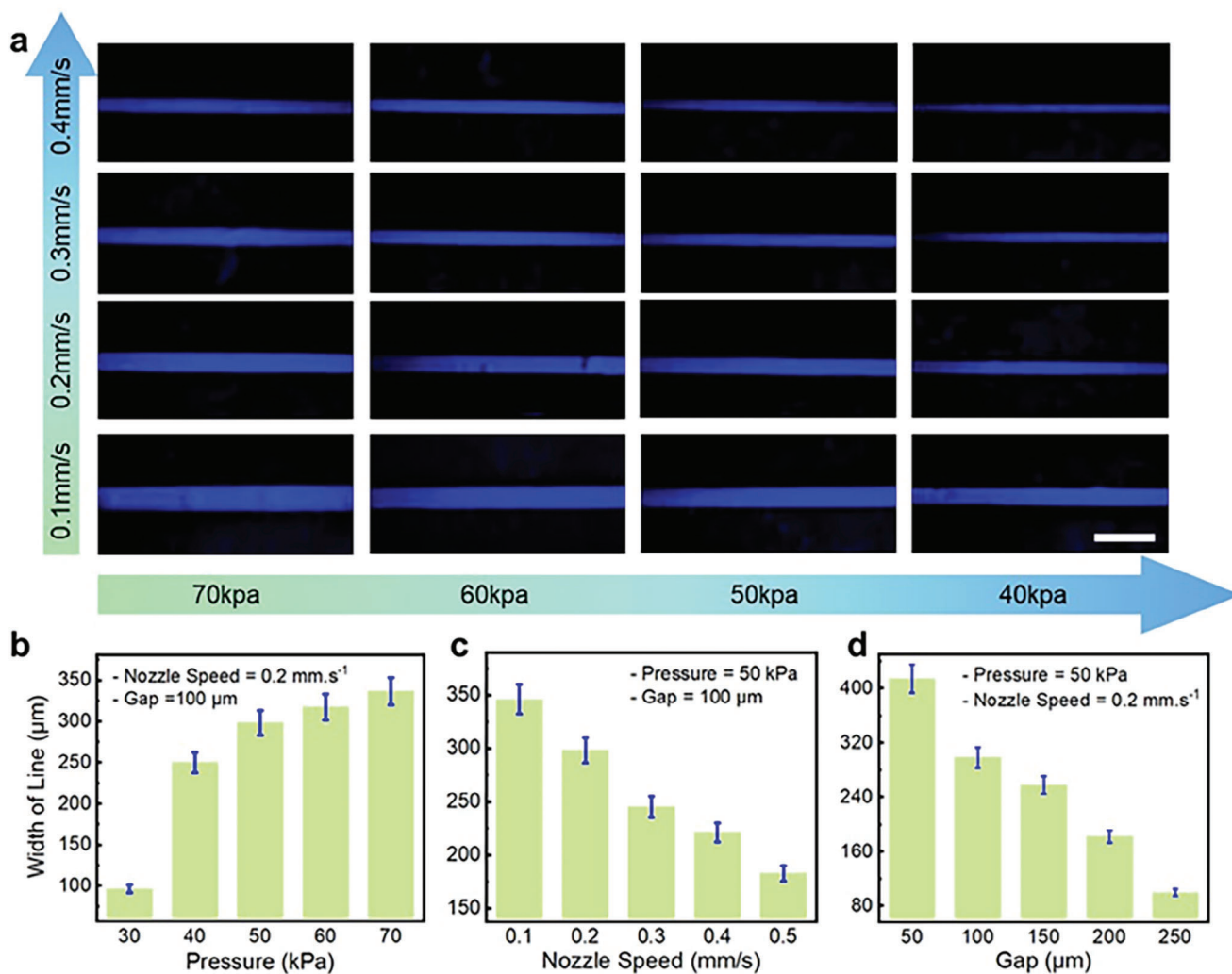
X-ray diffraction (XRD) of the PQD–polymer architectures showed pure cubic perovskite phases in relation to the halide ratio (**Figure 2a**). The XRD peaks were assigned to the (100), (110), (200), (210), (220), and (300) planes of $CH_3NH_3PbBr_3$ PQDs. The peaks observed are similar to those reported in previous studies on methylammonium lead halides.[3,55] These peaks shift toward lower diffraction angles with the addition of larger iodide anions and higher diffraction angles for smaller chloride anions, indicating a change in the lattice constants of the crystal cell.

XRD measurements confirmed that HPC was present in the PQD–polymer compositions. The optical properties of the fabricated PQD–polymer films were investigated using PL spectroscopy and UV–visible (Vis) absorption measurements, as shown in Figure 2b,c. The PL emission peaks and absorption onset exhibited a blue shift in the presence of chloride and a red shift with increasing iodide content. The PL emission peaks of the B-, G-, and R-emissive PQD–polymer showed single peaks at 467, 515, and 639 nm, with full width at half maximum changes of 20, 32, and 39 nm, respectively. The band gaps of B-, G-, and R-emissive PQD–polymer were ≈ 2.61, 2.42, and 1.89 eV based on the absorption spectra.

The color coordinates of the RGB PQD–polymer are presented as white circles in the Commission Internationale de l'Eclarage (CIE) chromaticity diagram (Figure 2d). The CIE coordinates of the B-emissive (0.190, 0.121), G-emissive (0.303, 0.540), and R-

emissive (0.593, 0.376) PQDs are shown in the CIE chart labeled 1. The color changes resulting from preparing RGB PQD–polymer compositions using varying amounts of PQDs in a constant amount of HPC solution (4 mL) are shown in color coordinates 2 and 3. The change in PQD concentration from 18.75, 37, to 51.75 mg mL^{-1} corresponded to the color coordinates 1, 2, and 3, respectively, producing a higher intensity of the PQD–polymer ink. The reduced PQD concentration compared to the constant volume of ink results in a decrease in the photoluminescent intensity due to the synthesis of ink via a planetary mixer. There was no apparent chemical or physical interaction between PQD and HPC; the HPC polymer was used for providing dispersion to the PQD in DCM.

Figure 2e,f shows the scanning electron microscopy (SEM) image with energy-dispersive X-ray spectroscopy (EDS) of the elemental mapping and energy spectrum results of the two overlapping line patterns, demonstrating a uniform G-emissive PQD-polymer composition distribution. EDS analysis of the elemental mapping and energy spectra for the R-emissive and B-emissive PQD–polymer is shown in Figures S4 and S5 (Supporting Information). The transmission electron microscopy (TEM) images as well as size distribution of $CH_3NH_3PbBr_{1.5}I_{1.5}$, $CH_3NH_3PbBr_3$, and $CH_3NH_3PbBr_{1.5}Cl_{1.5}$ are shown in Figure S3 (Supporting Information). The PQDs, which are typically diluted with toluene in the precursor and then centrifuged, have irregular spherical shapes. The TEM images show that CH3NH3PbBr1.5I1.5 QDs exhibits a particle size distribution with an average diameter of

ADVANCED
SCIENCE NEWS

www.advancedsciencenews.com

ADVANCED
FUNCTIONAL
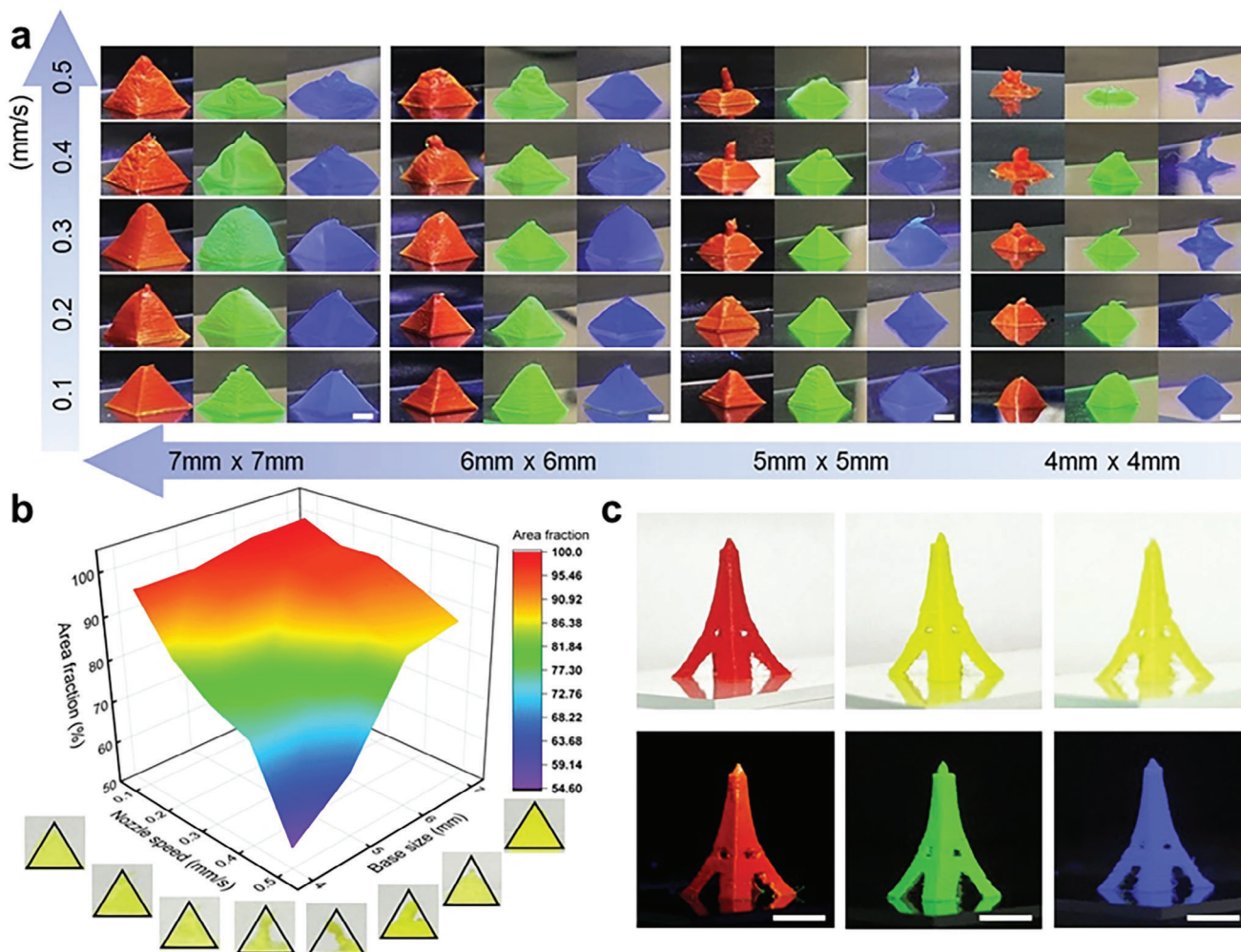**MATERIALS**

www.afm-journal.de

Figure 3. Characterization of printed B-emissive PQD–HPC patterns as functions of printing parameters. a) Optical graphs under daylight and UV of B-emissive PQD–HPC lines printed with a D_n of 150 µm and various nozzle speeds v_p (0.1, 0.2, 0.3, 0.4, and 0.5 mm s^{-1}) and pressure values P (30, 40, 50, 60, and 70 kPa). Ability to control the width of the printed line (W_P) with v_p and P. The scale bar is 1 mm. The dependence of the printed line W_P on b) P, c) v_p, and d) the gap between the glass substrate and the nozzle.

10.78 nm with a size deviation of ± 1.56 nm. CH3NH3PbBr3, and CH3NH3PbBr1.5Cl1.5 QDs have 9.08 nm ± 1.84 nm and 7.62 nm ± 1.56 nm, respectively. N-octylamine contributes to controlling the mechanism of crystallization for nanoparticles and preventing aggregation into large particles.[40,56–58]

The influence of printing parameters was further analyzed using DIW. **Figure 3**a shows the printability of the B-emissive PQD–polymer ink for 2D patterns visible under 385-nm UV-light excitation. The width of the printed patterns (W_P) was controlled by adjusting the printing parameters of printing speed, v_p (0.1, 0.2, 0.3, 0.4, and 0.5 mm s^{-1}), and applied pressure P (30, 40, 50, 60, and 70 kPa) using a nozzle diameter (D_n) of 150 µm. Consistently maintaining a uniform line width during layer-by-layer stacking enhances the printability of 3D structures. When the applied pressure is too low related to fast nozzle speed, a sequence of dots is formed upon contact with the substrate (Figure S6, Supporting Information). A dog bone-like shape is formed when the deposited line exhibits a smaller width than the droplets produced

after the ink was extruded initially.[59] As shown in Figure 3b, the change in P (30 to 70 kPa) shows an increasing W_P. Uniform printed lines W_P were obtained at approximately D_n of 150 µm under the printing condition of v_p = 0.2 mm s^{-1} and P = 50 kPa. The W_P of B-emissive PQD–polymer patterns decreased from 346.2 to 182.7 µm upon increasing v_p from 0.1 to 0.5 mm s^{-1}. The gap between the glass substrate and the nozzle also influences the W_P of the pattern (Figure 3d).

The 3D printability of the PL architecture is crucial for progressing the applications in printed electronics. **Figure 4**a shows the fabrication of a 3D pyramid of R-emissive, G-emissive, and B-emissive PQD–polymer through precise control of the micronozzle (D_n = 150 µm) in an LbL manner by DIW. Continuous ink extrusion is enabled by applying a pressure of 50 kPa and maintaining a layer height of 150 µm along the printing path. A series of 3D pyramids with varying square-base dimensions (S_Δ), including 4 mm (3.6 mm height), 5 mm (4.5 mm height), 6 mm (5.4 mm height), and 7 mm (6.3 mm height) were printed at

**ADVANCED
SCIENCE NEWS**

www.advancedsciencenews.com

**ADVANCED
FUNCTIONAL
MATERIALS**

www.afm-journal.de

Figure 4. a) Optical images depict the 3D printability of an R, G-, and B-emissive pyramid architecture for the layer-by-layer method using repetitive stacking via the micronozzle. 3D pyramids with various printing speeds v_p (0.1, 0.2, 0.3, 0.4, and 0.5 s^{-1}) and square-base dimensions S$_\Delta$ (4, 5, 6, and 7 mm) were prepared at a P of 50 kPa and layer gap of 150 µm. The scale bar is 2 mm. b) The area-fraction graph between the designed and printed shapes varies with the nozzle speed for each S$_\Delta$. The graph for S$_\Delta$ was created by examining the printed architecture for the design shape. c) Arbitrarily complex architecture of the Eiffel tower with R-, G-, and B-emissive PQD–HPC under daylight and 385-nm UV light. The scale bar is 5 mm.

printing speeds (v_p) of 0.1, 0.2, 0.3, 0.4, and 0.5 mm s^{-1}. At S$_\Delta$ = 7 mm, freestanding, 3D pyramids acquire a form at v_p values of 0.1, 0.2, and 0.3 mm s^{-1}. The rapid evaporation of DCM from the deposited ink led to solidification and retention of the 3D structure. As S$_\Delta$ decreased from 6 to 5 mm, the slow v_p of 0.1–0.2 mm s^{-1} printed the pyramids. An optimal printing speed can produce a 3D pyramid of the appropriate S$_\Delta$ dimension. A decrease in S$_\Delta$ does not lead to printing that produces a complete 3D architecture. As the S$_\Delta$ decreases to 4 mm, the minimum v_p also decreases to 0.1 mm s^{-1}. The optical images captured under natural light are presented in Figures S7 and S8 (Supporting Information). The printing time that completes the pyramid structure for 5 mm base is ≈ 2 h at 0.2 mm s^{-1}, which is the nozzle speed used to print a typical 3D structure. Figure 4b shows the variation in the area fraction for each S$_\Delta$ in increasing v_p. These were determined by dividing the area threshold of the front view of the designed shape in each image by the area threshold of the front view of the printed shape in each image. First, the pyra-

mid becomes triangular when observed in the front view. The procedure involved determining the area fraction of the triangle relative to a specified numerical value for the designed pyramid within a specific image size. Subsequently, a front-view photograph of the printed pyramid, acquired at the same image size, was analyzed for area fraction using the Image J software. By dividing the area fraction of the printed pyramid by that of the designed shape, the ratio indicating the occupied area of the printed shape compared to the design shape was determined. Figure S9 (Supporting Information) shows the calculation method for the area fraction. At low v_p, the attained area fraction is high due to continuous LbL stacking. At v_p = 0.1 mm s^{-1}, the S$_\Delta$ of 7 mm has an area fraction of 100%, which is consistent to 96.8% at S$_\Delta$ of 4 mm. As v_p was increased, the attained area fraction decreased for each S$_\Delta$. At v_p = 0.5 mm s^{-1}, the S$_\Delta$ of 7 mm has an area fraction of 88%, which is considerably decreased to 54.8% at S$_\Delta$ of 4 mm. The fast nozzle speed led to an inability to continuously stack owing to the thin printing pattern and die swelling owing
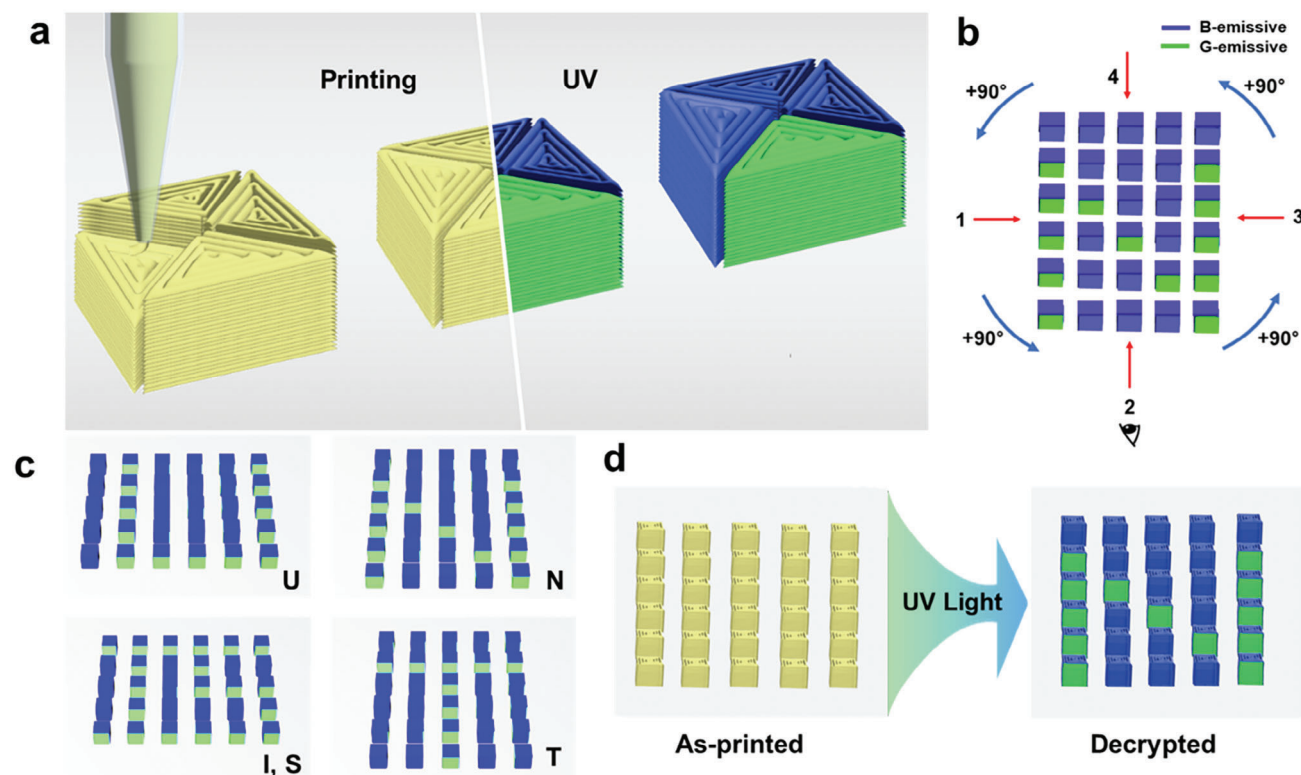
Figure 5. a) Illustration of printed bicolor anti-counterfeiting cubic architectures comprising triangular units. b) Schematic design of a 6 × 5 3D array consisting of G- or B-emissive PQD–HPC on individual cube faces. The array sides encrypt information, with the denoting at 90° counterclockwise intervals. c) Design of a collective encryption of alphabets (U, N, I, S, T) as viewed from the top. The decryption in an inclined view of each array side, denoting U, N, IS, and T letters. d) Illustration of 3D printed 6 × 5 array cubic architectures under daylight and 385-nm UV light. The as-printed array decrypts information under UV light.
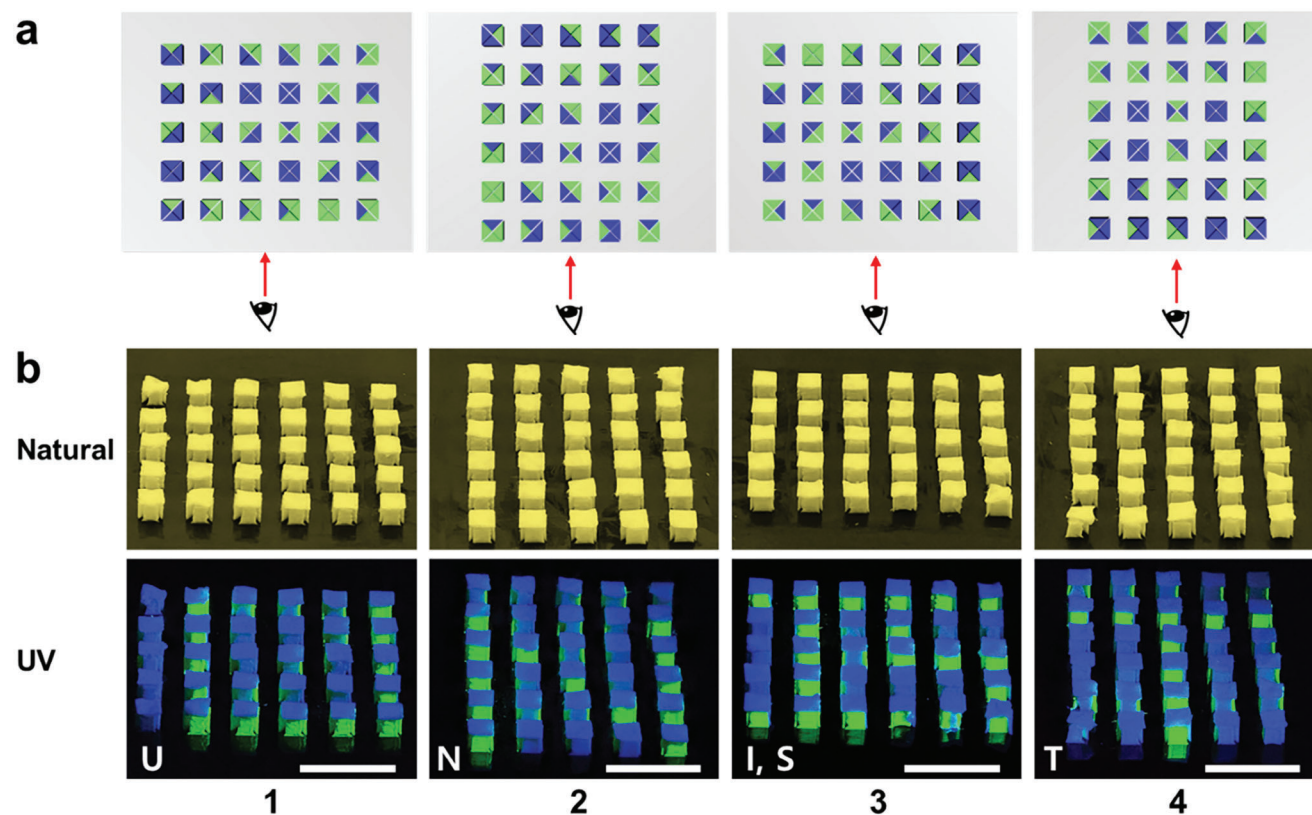
to contact with the nozzle before complete solidification of the ink.

The PQD-composites contribute to the stability of maintaining the photoluminescent function of PQD. Stability tests were conducted to determine whether pyramid structures at both room temperature and 80 °C heat plate could retain their photoluminescence after 150 h. In Figure S10 (Supporting Information), G-emissive pyramid showed a dim green light, which maintained their luminescence in the room temperature. However, their intensity was reduced at 80 °C after 150 h. The luminescence of B-pyramid decreased significantly without color change after 150 h at both the room temperature and 80 °C. Rapid oxidation and decomposition in iodide ions lead to poor chemical stability and degradation of their photoluminescent performance. The initial ink exhibits a red light, which decreases in luminescent functionality after 150 h. R-emissive pyramid exposed to 80 °C heat plate showed a bright orange color.

Figure 4c shows the illuminated optical images under daylight and 385-nm UV light of the as-fabricated Eiffel tower architectures in R-, G-, and B-emissive PQD-polymers with Eiffel tower base dimensions of 8 mm (height = 12 mm). The LbL printing of the micronozzle track movement was controlled by applying a pressure of 50 kPa and v_p of 0.2 mm s^{-1} to allow ink to feature uniform line patterns. Printing Eiffel tower shapes at 6- and 7-mm bases did not result in successful LbL stacking and led to die swelling in the upper part (Figure S11, Supporting Informa-

tion). The Eiffel tower architectures were uniform, with continuous stacking for Eiffel tower base dimensions of 8 mm. This is an effective approach to fabricate intricate architectures, as indicated by the uniform and accurate Eiffel tower architectures obtained in this study.

The ability to emit specific colors under UV light is widely used in high-precision security techniques. PQDs can emit different colors in 385-nm UV light and can provide anti-counterfeiting and information-encryption features. As shown in **Figure 5**, the capability to print complex architectures arbitrarily offers diversity in anti-counterfeiting blocks, leading to highly secure anti-counterfeiting technologies. We fabricated 6 × 5 blocks that displayed alphabetic letters at different angles. Figure 5a shows a schematic of the 3D printing of bicolor anti-counterfeiting cubic architectures containing triangular units. These square blocks are composed of four triangular units that represent bicolor. 3D anti-counterfeiting architectures were developed to display alphabetic letters at 90° counterclockwise intervals, as shown in Figure 5b. When observed as a whole and rotated 90° sequentially, the letters U, N, IS, and T were observed (Figure 5c). Figure 5d shows a schematic illustration of a 3D printed 6 × 5 array cubic architecture under daylight and 385-nm UV light. The as-printed array could decrypt information when exposed to UV light. A thin layer of B-emissive ink was overprinted above the array of cubic architectures to tilt the blocks and make the letters appear more accurate. Without overprinting, green

**ADVANCED
SCIENCE NEWS**

www.advancedsciencenews.com

**ADVANCED
FUNCTIONAL
MATERIALS**

www.afm-journal.de

Figure 6. a) Schematic of a bicolor anticounterfeit 3D cubic array with G- and B-emissive PQD–HPC for the decryption of each array side, denoting letters U, N, IS, and T. b) Optical images observed under daylight and 385-nm UV light to represent the letters U, N, IS, and T. The scale bar is 2 cm.

structures of other angles are observable, presenting difficulties in distinguishing the "N" letter (Figure S12, Supporting Information).

Figure 6a depicts a 3D cubic array designed to prevent counterfeiting, with two different colors used for identification. The production of various structures through the stacking of perovskites features a luminescent color that is produced through 3D printing, determined by the composition, and can serve as an anti-counterfeiting label. The ability to build a structure via LbL stacking opens up possibilities for creating diverse information and security systems, extending beyond simple UV encryption and decryption when viewed from a multifaceted perspective. We demonstrated a simple 3D cubic array to illustrate a label capable of accommodating two pieces of information (Figure S13, Supporting Information). Subsequently, we progressively expanded their capabilities to 3D multifaceted perspectives, developing anti-counterfeiting arrays with an increasing capacity for storing information. The array utilizes G- and B-emissive PQD-HPC to decrypt each side of the cube, which represents the letters U, N, IS, and T. In Figure 6b, the printed anti-counterfeiting labels display alphabetic letters for UNIST at 90° intervals. The figure shows "U" at 0°, "N" at 90°, "IS" at 180°, and "T" at 270°. The observation of anti-counterfeiting labels with the unaided eye reveals a pale-yellow array, posing challenges in discerning finer details. However, when illuminated with UV light, they emit G and B colors, respectively, allowing easy recognition of these letters. The results demonstrate that the proposed anticounterfeit ar-

ray provides a method for enhancing the capabilities of information storage and encryption applications. The diversity of heights and angles in 3D structures facilitates the encryption and anti-counterfeiting of their own information. Furthermore, R-, G-, and B-emissive PQDs can be used to print arbitrary architectures to improve the security level with the diversity of 3D-printed luminescent PQDs.

3. Conclusion

We explore the fabrication of 3D PQD–polymer architectures with arbitrary and complex shapes. Centrifuged PQD from the synthesized precursor, according to the halide ratio, emitted RGB colors, and the ink was formulated for rheologically stable extrusion with HPC and DCM. The effective printing of complex architectures is demonstrated by determining the 3D printability of DIW. Specific conditions under which the PQD–HPC ink exhibited consistent stacking were identified, resulting in the successful printing of a uniform Eiffel tower structure. Furthermore, this study introduces potential applications of 3D-printed PQD–HPC architectures in anti-counterfeiting technologies. The ability of PQDs to emit specific colors under UV light is leveraged to create anti-counterfeiting arrays that offer diverse security features. The design of a 6 × 5 cube architecture array used G- and B-emissive PQD–HPCs for encryption to display letters (U, N, IS, and T) at 90° intervals. Overall, the established 3D-printing method employing luminescent PQDs functional inks

opens new avenues for creating complex encryption applications. Building more complex structures and arrays beyond the demonstrated 3D cube array could provide additional information. The capacity for data storage and encryption can be improved by expanding the range of the compositional combinations. Multiple, bicolor-3D architectures have been presented as encryption applications to enhance modern printed electronic devices.

4. Experimental Section

Synthesis of $CH_3NH_3PbBr_3$, $CH_3NH_3PbBr_{1.5}Cl_{1.5}$, *and* $CH_3NH_3PbBr_{1.5}I_{1.5}$ *PQDs*: To synthesize $CH_3NH_3PbBr_3$ PQDs, a clear precursor solution was prepared by adding CH_3NH_3Br (0.4 mmol, 99%, GreatCell Solar) and $PbBr_2$ (0.3 mmol, 99%, Sigma–Aldrich) in a mixed solvent composed of DMF (1 mL; anhydrous 99.8%, Sigma–Aldrich), GBL (17 mL; ≥99.5%, Samchun Chemicals), and n-octylamine (40 µL; 99%, Sigma–Aldrich) at room temperature using a vortex mixer (VM-30; Daihan Scientific Co.). Next, 1 mL of the precursor solution was vigorously stirred in toluene (20 mL, 99.9%, Sigma–Aldrich). The colloidal solution was centrifuged (MAXpin C-12mt; Daihan Scientific Co.) at 5000 rpm for 10 min to remove precipitates. The PQDs were collected by centrifugation at 13 500 rpm for 10 min. $CH_3NH_3PbBr_{1.5}Cl_{1.5}$ PQDs or $CH_3NH_3PbBr_{1.5}I_{1.5}$ PQDs were synthesized by combining the perovskite precursor solutions in equal ratios. The precursor solution of $CH_3NH_3PbBr_{1.5}Cl_{1.5}$ required an additional quantity of dimethyl sulfoxide (2 mL; 99.5%, Samchun Chemicals) solvent to dissolve the $PbCl_2$ and CH_3NH_3Cl.

Preparation of Composite Ink with PQD–HPC: The PQD–HPC ink was prepared by adding 200 mg of G, R, and B PQDs to a mixture of HPC (0.2 g; 99%, Mw ≈ 100 000, Sigma–Aldrich) in DCM (2 mL; 99.5%, Sigma Aldrich) at 25 °C in a mixer (ARE-310; THINKY Co.). The rheological properties of the ink were characterized using a rheometer (Haake MARS III, ThermoElectron) with a parallel-plate configuration. Strain sweeps ranging from 10^0 to 10^2 s^{-1} were performed to measure the ink viscosity at different shear rates, while it was performed at a consistent frequency of 1 Hz to record the changes in the storage (G') and loss (G″) moduli of the ink in response to varying stress level.

PQD–HPC Architectures: The 3D architectures of PQD–HPC were fabricated using a fluid dispenser (ML-808GX, Musashi Engineering Inc.). The ink loaded into a syringe (3 mL barrel, Musashi Engineering Inc.) was extruded through a micronozzle (ID = 150 µm). The speed and nozzle position were controlled using a three-axis motion platform (SHOTmini 200SX, Musashi Engineering Inc.), and the motion corresponding to the print path was designed using customized computer-aided design (CAD) software (MuCAD V, Musashi Engineering Inc.). The 3D models were designed using CAD software (Solidworks, Dassault Systèmes) and converted into the standard tessellation language format, followed by slicing the model to generate G-code coordinates. The G-code was then converted into the MuCAD V command language using a custom-written Python program.

Characterizations: XRD analysis was performed at a scanning speed of 0.15 s/step with Cu Kα radiation (λ = 0.154 nm) from X-ray source (D8 Advance, Bruker AXS) operated at 40 mA. The UV–vis absorption spectra were acquired using a UV–vis–NIR spectrophotometer (Cary 5000, Agilent Technologies) to study the optical absorption of the $CH_3NH_3PbX_3$ PQD–HPC films. The PL spectra were measured using a spectrofluorometer (FP-8500ST, Jasco International) with a xenon lamp (150 W) as the irradiation source. The microscopic characteristics and elemental compositions of the printed PQD–HPC architectures were analyzed using field-emission SEM (SU8220, Hitachi). The nanostructure of the PQDs was analyzed using a Normal-TEM (JEM-2100, JEOL).

Supporting Information

Supporting Information is available from the Wiley Online Library or from the author.

Conflict of Interest

The authors declare no conflict of interest.

Data Availability Statement

The data that support the findings of this study are available in the supplementary material of this article.

[1] Q. V. Le, K. Hong, H. W. Jang, S. Y. Kim, *Adv. Electron. Mater.* **2018**, *4*, 1800335.

[2] H. C. Wang, Z. Bao, H. Y. Tsai, A. C. Tang, R. S. Liu, *Small* **2018**, *14*, 1702433.

[3] F. Zhang, H. Zhong, C. Chen, X. Wu, X. Hu, H. Huang, J. Han, B. Zou, Y. Dong, *ACS Nano* **2015**, *9*, 4533.

[4] L. C. Schmidt, A. Pertegás, S. González-Carrero, O. Malinkiewicz, S. Agouram, G. M. Espallargas, H. J. Bolink, R. E. Galian, J. Pérez-Prieto, *J. Am. Chem. Soc.* **2014**, *136*, 850.

[5] H. Huang, A. S. Susha, S. V. Kershaw, T. F. Hung, A. L. Rogach, *Adv. Sci.* **2015**, *2*, 581.

[6] M. Cha, P. Da, J. Wang, W. Wang, Z. Chen, F. Xiu, G. Zheng, Z. Wang, *J. Am. Chem. Soc.* **2016**, *138*, 8581.

[7] S. S. Mali, C. S. Shim, C. K. Hong, *NPG Asia Mater* **2015**, *7*, e208.

[8] Y. H. Kim, C. Wolf, Y. T. Kim, H. Cho, W. Kwon, S. Do, A. Sadhanala, G. P. Chan, S. W. Rhee, H. I. Sang, *ACS Nano* **2017**, *11*, 6586.

[9] J. Xing, F. Yan, Y. Zhao, S. Chen, H. Yu, Q. Zhang, R. Zeng, H. V. Demir, X. Sun, A. Huan, Q. Xing, *ACS Nano* **2016**, *10*, 6623.

[10] Y. Liu, Y. Zhang, Z. Yang, D. Yang, X. Ren, L. Pang, S. Liu, *Adv. Mater.* **2016**, *28*, 9204.

[11] J. Ghosh, R. Ghosh, P. K. Giri, *ACS Appl. Mater. Interfaces* **2019**, *11*, 14917.

[12] K. Wang, Y. Du, J. Liang, J. Zhao, F. F. Xu, X. Liu, C. Zhang, Y. Yan, Y. S. Zhao, *Adv. Mater.* **2020**, *32*, 2001999.

[13] X. Zhang, X. Liu, B. Sun, H. Ye, C. He, L. Kong, G. Li, Z. Liu, G. Liao, *ACS Appl. Mater. Interfaces* **2021**, *13*, 35949.

[14] X. Wang, M. Shoaib, X. Wang, X. Zhang, M. He, Z. Luo, W. Zheng, H. Li, T. Yang, X. Zhu, L. Ma, A. Pan, *ACS Nano* **2018**, *12*, 6170.

[15] G. Wang, D. Li, H. Cheng, Y. Li, C. Chen, A. Yin, Z. Zhao, Z. Lin, H. Wu, Q. He, M. Ding, Y. Liu, Y. Huang, X. Duan, *Sci. Adv.* **2015**, *1*, 1500613.

[16] X. Liu, L. Niu, C. Wu, C. Cong, H. Wang, Q. Zeng, H. He, Q. Fu, W. Fu, T. Yu, C. Jin, Z. Liu, T. C. Sum, *Adv. Sci.* **2016**, *3*, 1600137.

[17] J. Feng, X. Yan, Y. Zhang, X. Wang, Y. Wu, B. Su, H. Fu, L. Jiang, *Adv. Mater.* **2016**, *28*, 3732.

[18] P. Liu, X. He, J. Ren, Q. Liao, J. Yao, H. Fu, *ACS Nano* **2017**, *11*, 5766.

[19] B. Jeong, I. Hwang, S. H. Cho, E. H. Kim, S. Cha, J. Lee, H. S. Kang, S. H. Cho, H. Choi, C. Park, *ACS Nano* **2016**, *10*, 9026.

[20] S. Chen, K. Roh, J. Lee, W. K. Chong, Y. Lu, N. Mathews, T. C. Sum, A. A. Nurmikko, *ACS Nano* **2016**, *10*, 3959.

[21] W. Deng, L. Huang, X. Xu, X. Zhang, X. Jin, S. Lee, J. Jie, *Nano Lett.* **2017**, *17*, 2482.

[22] Z. Gu, Z. Zhou, Z. Huang, K. Wang, Z. Cai, X. Hu, L. Li, M. Li, Y. S. Zhao, Y. Song, *Adv. Mater.* **2020**, *32*, 1908006.

[23] D. N. Minh, S. Eom, L. A. T. Nguyen, J. Kim, J. H. Sim, C. Seo, J. Nam, S. Lee, S. Suk, J. Kim, Y. Kang, *Adv. Mater.* **2018**, *30*, 1802555.

[24] C. H. Lin, Q. Zeng, E. Lafalce, S. Yu, M. J. Smith, Y. J. Yoon, Y. Chang, Y. Jiang, Z. Lin, Z. V. Vardeny, V. Tsukruk, *Adv. Opt. Mater.* **2018**, *6*, 1800474.

[25] T. Hu, M. Zhang, H. Mei, P. Chang, X. Wang, L. Cheng, *Adv. Mater. Technol.* **2023**, *8*, 2200827.

[26] Y. Zhu, T. Tang, S. Zhao, D. Joralmon, Z. Poit, B. Ahire, S. Keshav, A. R. Raje, J. Blair, Z. Zhang, X. Li, *Addit. Manuf.* **2022**, *52*, 102682.

[27] A. Camposeo, L. Persano, M. Farsari, D. Pisignano, *Adv. Opt. Mater.* **2019**, *7*, 1800419.

[28] J. A. Lewis, B. Y. Ahn, *Nature* **2015**, *518*, 42.

[29] Y. L. Kong, I. A. Tamargo, H. Kim, B. N. Johnson, M. K. Gupta, T. Koh, H. Chin, D. A. Steingart, B. P. Rand, M. C. McAlpine, *Nano Lett.* **2014**, *14*, 7017.

[30] K. Sun, T. Wei, B. Y. Ahn, J. Y. Seo, S. J. Dillon, J. A. Lewis, *Adv. Mater.* **2013**, *25*, 4539.

[31] K. Fu, Y. Wang, C. Yan, Y. Yao, Y. Chen, J. Dai, S. Lacey, Y. Wang, J. Wan, T. Li, Z. Wang, Y. Xu, L. Hu, *Adv. Mater.* **2016**, *28*, 2587.

[32] Y. Yao, K. K. Fu, C. Yan, J. Dai, Y. Chen, Y. Wang, B. Zhang, E. Hitz, L. Hu, *ACS Nano* **2016**, *10*, 5272.

[33] F. Ning, W. Cong, J. Qiu, J. Wei, S. Wang, *Composites, Part B* **2015**, *80*, 369.

[34] Y. Tang, B. Liu, H. Yuan, Y. Xin, X. Ren, Q. Chen, H. Yin, *J. Alloys Compd.* **2022**, *916*, 164961.

[35] C. Tai, W. Hong, Y. Kuo, C. Chang, M. Niu, M. K. P. Ochathevar, C. Hsu, S. Horng, Y. Chao, *ACS Appl. Mater. Interfaces* **2019**, *11*, 30176.

[36] C. D. Brubaker, T. M. Frecker, J. R. McBride, K. R. Reid, G. K. Jennings, S. J. Rosenthal, D. E. Adams, *J. Mater. Chem. C* **2018**, *6*, 7584.

[37] E. García-Tuñon, S. Barg, J. Franco, R. Bell, S. Eslava, E. D'Elia, R. C. Maher, F. Guitian, E. Saiz, *Adv. Mater.* **2015**, *27*, 1688.

[38] X. Liang, H. Li, J. Dou, Q. Wang, W. He, C. Wang, D. Li, J. Lin, Y. Zhang, *Adv. Mater.* **2020**, *32*, 2000165.

[39] S. K. Seol, D. Kim, S. Lee, J. H. Kim, W. S. Chang, J. T. Kim, *Small* **2015**, *11*, 3896.

[40] D. W. Yee, M. A. Citrin, Z. W. Taylor, M. A. Saccone, V. L. Tovmasyan, J. R. Greer, *Adv. Mater. Technol.* **2020**, *6*, 2000791.

[41] Q. L. Zhu, C. Du, Y. Dai, M. Daab, M. Matejdes, J. Breu, W. Hong, *Nat. Commun.* **2022**, *11*, 5166.

[42] X. Yang, C. Valenzuela, X. Zhang, Y. Chen, Y. Yang, L. Wang, W. Feng, *Matter* **2023**, *6*, 1278.

[43] M. Wajahat, J. H. Kim, J. H. Kim, I. D. Jung, J. Y. Pyo, S. K. Seol, *ACS Appl. Mater. Interfaces* **2023**, *15*, 59582.

[44] T. Xuan, S. Guo, W. Bai, T. Zhou, L. Wang, R. Xie, *Nano Energy* **2022**, *95*, 107003.

[45] L. F. Shi, L. H. Meng, F. Jiang, Y. Ge, F. Li, X.-g. Wu, H. Z. Zhong, *Adv. Funct. Mater.* **2019**, *29*, 1903648.

[46] J. Chen, Y. Wu, X. M. Li, F. Cao, Y. Gu, K. Liu, X. H. Liu, Y. H. Dong, J. P. Ji, H. B. Zeng, *Adv. Mater. Technol.* **2017**, *2*, 1700132.

[47] S. Pan, Y. Chen, Z. Wang, Y. Harn, J. Yu, A. Wang, M. J. Smith, Z. Li, V. V. Tsukruk, J. Peng, Z. Lin, *Nano Energy* **2020**, *77*, 105043.

[48] M. Kim, I. D. Jung, Y. Kim, J. Yun, C. Gao, H. Lee, S. W. Lee, *Sens. Actuators, B* **2020**, *322*, 128601.

[49] I. D. Jung, M. Kim, C. Gao, Y. Liu, C. Park, H. Lee, S. W. Lee, *Nano Lett.* **2020**, *20*, 1800.

[50] J. H. Kim, S. Park, J. Ahn, J. Pyo, H. Kim, N. Kim, I. D. Jung, S. K. Seol, *Adv. Sci.* **2023**, *10*, 2205588.

[51] R. Xu, C. Qiao, C. Mia, B. Bai, Y. Li, J. Liu, J. Liu, H. Rong, M. Xu, J. Zhang, *J. Mater. Chem. C* **2021**, *9*, 7194.

[52] M. Chen, J. Yang, Z. Wang, Z. Xu, H. Lee, H. Lee, Z. Zhou, S. Feng, S. Lee, J. Pyo, S. K. Seol, D. Ki, J. T. Kim, *Adv. Mater.* **2019**, *31*, 1904073.

[53] M. Chen, Z. Zhou, S. Hu, N. Huang, H. Lee, Y. Liu, J. Yang, X. Huan, Z. Xu, S. Cao, X. Cheng, T. Wang, S. F. Yu, B. P. Chan, J. Tang, S. P. Feng, J. T. Kim, *Adv. Funct. Mater.* **2023**, *33*, 2212146.

[54] S. Hu, X. Huan, J. Yang, H. Cui, W. Gao, Y. Liu, S. F. Yu, H. C. Shum, J. T. Kim, *Nano Lett.* **2023**, *23*, 9953.

[55] L. Peng, A. Tang, C. Yang, F. Teng, *J. Alloys Compd.* **2016**, *687*, 506.

[56] H. S. Yang, S. H. Noh, E. H. Suh, J. Jung, J. G. Oh, K. H. Lee, J. Jang, *ACS Appl. Mater. Interfaces* **2021**, *13*, 4374.

[57] J. Enomoto, R. Sato, M. Yokoyama, T. Kimura, N. Oshita, K. Umemoto, S. Asakuraab, A. Masuhara, *RSC Adv.* **2022**, *12*, 5571.

[58] Z. Zhenfu, J. Liang, W. Zhihai, C. Jiong, Z. Miaomiao, H. Yafei, *J. Mater. Sci.* **2018**, *53*, 15430.

[59] J. B. Kim, C. Chae, S. H. Han, S. Y. Lee, S. Kim, *Sci. Adv.* **2021**, *7*, 48.